Imaging protein structure in water at 2.7 nm resolution by TEM

Utkur M. Mirsaidov,[† ‡] Haimei Zheng,[§] Yosune Casana,[‡] Paul Matsudaira,[† ‡]

[†] Mechanobiology Institute, National University of Singapore, 5A Engineering Drive 1, Singapore, 117411;
[‡] Center for BioImaging Sciences, Department of Biological Sciences, National University of Singapore, Science Drive 4, Singapore, 117557;
[§] Materials Science Division, Lawrence Berkeley National Laboratory, Berkeley, CA;

correspondence to: dbsmpt@nus.edu.sg

Supporting Material

Supplementary Methods:

Protein samples: Acrosomal bundles were purified from the sperm of horseshoe crab, *Limulus polyphemus* as described by Schmid et al. (1). The resulting acrosome solution was diluted 1:5 in pure water, loaded into a liquid cell, and sealed with vacuum grease to a copper gasket. MAP-Rich microtubule protein (MTP) was purified as described by Wilson and coworkers (2). A 2 mg/ml solution of MTP in PEMG buffer (100 mM Pipes, 1 mM EGTA, 1 mM $MgSO_4$, and 1 mM GTP at pH 6.8) was incubated at 30^{o}C for 30 min. to form self-nucleating microtubules. Taxol (20 µM) was then added to stabilize the microtubules. Stable microtubules were diluted 1:1 in pure water before loading into the liquid cell.

Experimental procedures: A low stress silicon nitride film (Si_3N_4) was deposited by LPCVD to a thickness of 10-25 nm on 300 µm thick 4 inch wafers (Ultrasil, Hayward, CA). The features of the 425 µm x 475 µm liquid cell were patterned by photolithography to form a ~3 x 50 µm window flanked by a pair of liquid reservoirs on one chip (top), and membrane window and 80-450 nm thick indium spacer on a second chip (bottom) using a stepper mask. After plasma cleaning ($P=3.3\ W$) for 45 s the two pieces were aligned by their windows and bonded together at 125°C for 2 hrs to form a single liquid chamber. Plasma cleaning is essential for flowing protein solutions in a narrow gap between the membranes. Microtubules (25 nm in diameter) were imaged in 80 nm-thick chambers while ~100 nm diameter acrosomes were imaged in ~200 nm thick chambers. The liquid cell was then placed into single-tilt holder and imaged at 120 keV in an FEI Technai T12 TEM. The dose rate was measured with a built-in and calibrated Faraday cup prior to the first image and verified at the end of the time series.

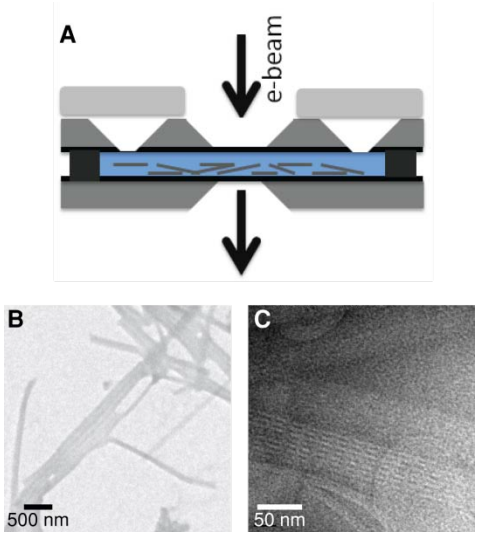

Figure S1: Overview of the setup. (A) After assembly and glow discharge, the liquid cell is loaded with the solution containing proteins and capped with copper gasket where vacuum grease served as sealant between the liquid cell and gasket. (B) After locating the Si_3N_4 window under the electron beam we image at low magnification to locate a suitable field of acrosomes. (C) Images of acrosomes for structure analysis are then taken at 30,000X magnifications and under low electron dose conditions. Scale bars are 50 nm.

Imaging: Each image was recorded with a Gatan Ultrascan 4096 x 4096 pixel camera at a nominal microscope magnification of 26,000-30,000X and at 1.5 µm defocus. The specimen dose for each frame was 5 e/A^2 with a cumulative dose of 100 e/A^2 for twenty images taken in liquid cell and 7 e/A^2 for vitrified samples. The exposure time was 1 s. We chose to analyze the distinctive *h0l* projection of the acrosomal bundle sample due to its distinct pattern. Identical size areas from images of a series were boxed (1020 x 280 pixels) and a Fourier transform of each boxed area was calculated. The data were processed using the MRC 2D crystal processing package (1, 3). The Fourier transforms of the acrosomal bundle images were indexed manually, followed by and refinement of the reciprocal lattice to obtain the unit cell parameters in Fourier space. A list of amplitudes corresponding to SNR $\geq$ 1.2 ($IQ \leq 6$) was considered for radiation damage analysis. Radiation damage plot showing relative amplitude versus electron dose was

generated by summing the amplitudes of all the Fourier peaks in a given resolution shell and by normalizing the summed amplitudes with respect to the first image. The relative contrast and the intensity of the electron micrographs were not adjusted for acrosomal bundle images. Contrast was enhanced for microtubules shown in Figure 1F of the main text for visual purposes.

Supporting Discussion:

Resolution versus membrane thickness: In ideal TEM imaging, resolution is governed by beam broadening and chromatic aberrations. Beam broadening, *b*, of a coherent electron beam is caused by elastic scattering of electrons by specimen atoms and defined by Goldstein (4):

$$b = 8 \times 10^{-12} \frac{Z}{E_0} N_V^{1/2} t^{3/2} \text{ (Eq. S1)}$$

Here, Z is atomic number, E_0 is beam energy in the units of keV (for our study: E_0=120 keV), N_v is the number of atoms per m^3 and t is the thickness of Si_3N_4. Resolution limitation due to chromatic aberration, on the other hand, is a result of inelastic scattering or energy loss of electrons as incoming electron interacts with the specimen's atom and given by (5):

$$r_{ch} = C_c \frac{\Delta E}{E_0} \beta \quad \text{(Eq. S2)}$$

where C_c = 2.2 mm is the chromatic aberration coefficient of the image forming lens, β = 11 mrad is the semi-angle of the objective aperture, E_0 is the energy of an incident electron and ΔE is the energy loss by electron due to an inelastic scattering. As a beam of electrons with energy E passes through a material of thickness dx, inelastic interactions result in energy loss of electron by amount of dE given by Bethe function (5):

$$-\frac{dE}{dx} = 2\pi N_0 e^4 \rho \frac{Z}{AE} \ln \frac{aE}{I} \quad \text{(Eq. S3)}$$

where A is the gram atomic weight of the material, N_0 is Avogadro's number, e is the electron charge, ρ is the density of the material, I is the mean excitation energy for energy loss in the

material and can be approximated as $I=(9.76Z + 58.8/Z^{1.19})$ and a is constant with the value of 1.16 for relativistic energy electrons. Z values for water and Si_3N_4 are $(2/3x1^2+1/3x8^2)^{1/2}=4.7$ and $(3/7x14^2+4/7x7^2)^{1/2}=10.6$ respectively. An energy filter could minimize the chromatic aberration by reducing ΔE, but at the expense of imaging at higher doses because the image intensity is also reduced.

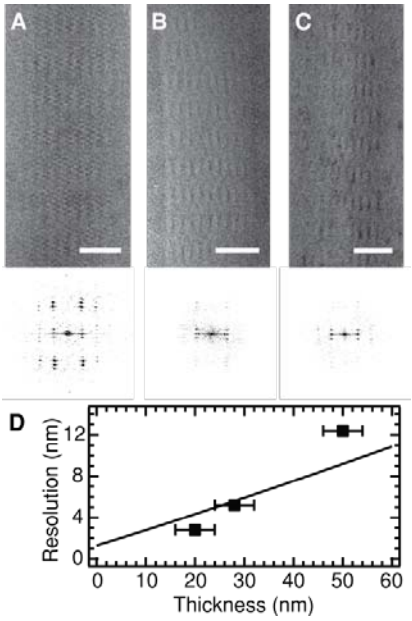

Figure S2: Resolution as a function of combined window thickness. Micrographs (upper) and Fourier transforms (lower) of the acrosomal bundle imaged through the liquid cell window with a Si_3N_4 membrane thickness of (A) 10 nm, (B) 14 nm, and (C) 25 nm. The Fourier transforms and resolution plot versus the membrane thickness (D) show the amount of information increases as the window thickness decreases. The theoretical estimate for idealized resolution limit which is the sum of equations (S1) and (S2) is plotted for comparison (solid line). The water thickness is ~200 nm and a defocus value of ~1.5 µm is used in all cases. The scale bars are 50 nm.

To a first approximation the sum of beam broadening and chromatic aberrations given in equations (S1) and (S2) should define the extent of our resolution. When plotted alongside the measured resolution (Figure S2D), the resolution limit at zero window thickness is 1.2 nm. Thus, future improvements to the liquid cell will be realized from thinner and/or more electron-transparent windows.

Membrane Transmittance: Before electrons can reach the protein sample it must pass through the top membrane window. Our electron dose values reported in Figure 2 of the main text reflect the corrected values for the electrons transmitted through the membrane window (Figure S3).

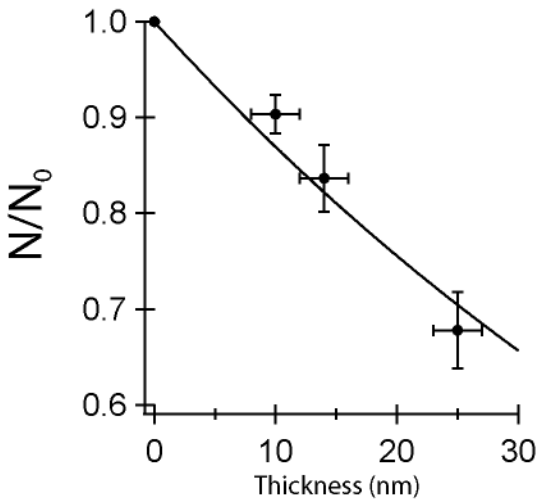

Figure S3: Transmittance of 120 keV beam through a Si_3N_4 membrane as a function of membrane thickness. Solid line is an exponential fit.

Radiation Damage: Figure 2 in the main text of the manuscript plots radiation damage as a function of the electron dose. Here we observe that zig-zag patterns start to vanish earlier in the case of frozen samples imaged at 98 K than in the aqueous samples imaged at room temperature (Figure S4-5). Low image contrast in the aqueous sample is mainly due to the background contribution from the membrane. Along with the images we also display the Fourier transforms of the selected regions that were used to obtain the Fourier amplitudes and *IQ* values. Although adsorbed to the membrane surface, the acrosomal bundle can drift and flex in water (see image taken at 100 e/A^2). In vitrified samples, drift and displacement arise from specimen and ice charging.

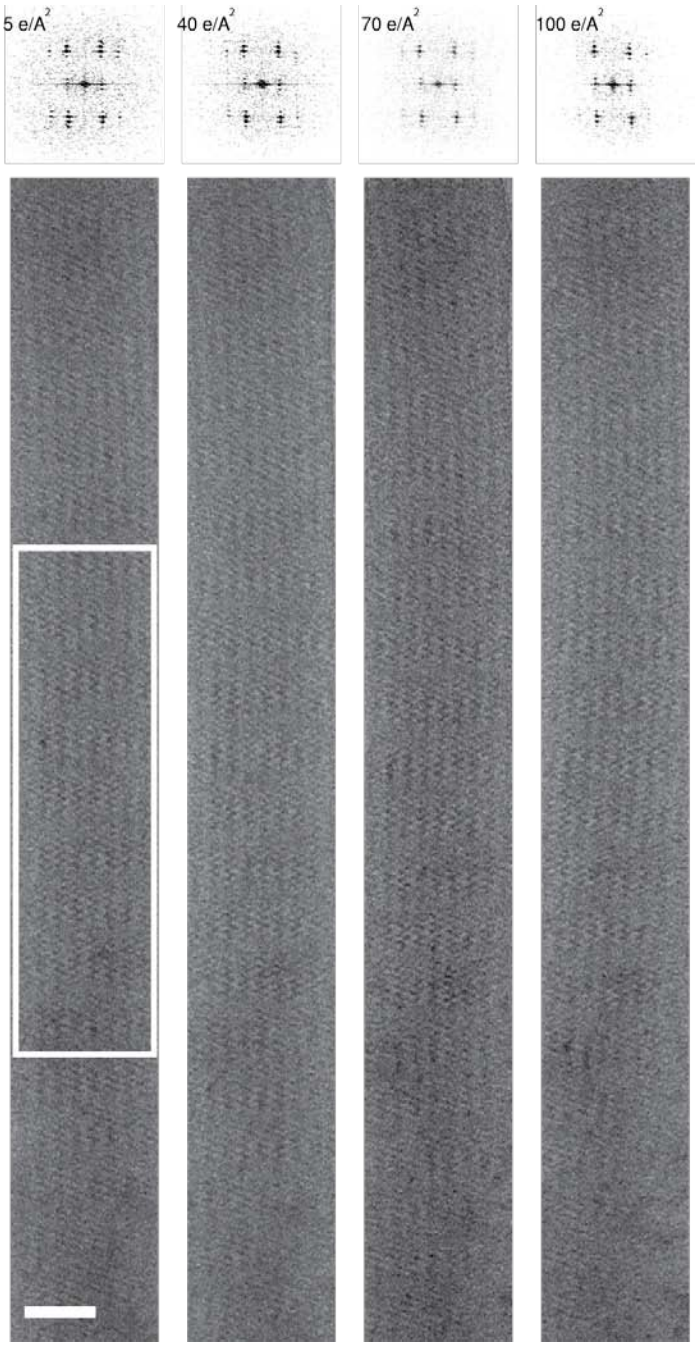

Figure S4: Corresponding images for the room temperature water data presented in Figure 2 of the main text. During the imaging in liquid water we observe both drift and bending of the acrosomal bundle while the zig-zag pattern remains. This floating is due to poor adhesion of the protein to a membrane window. The Fourier transform was taken from the boxed area. The scale bar is 50 nm.

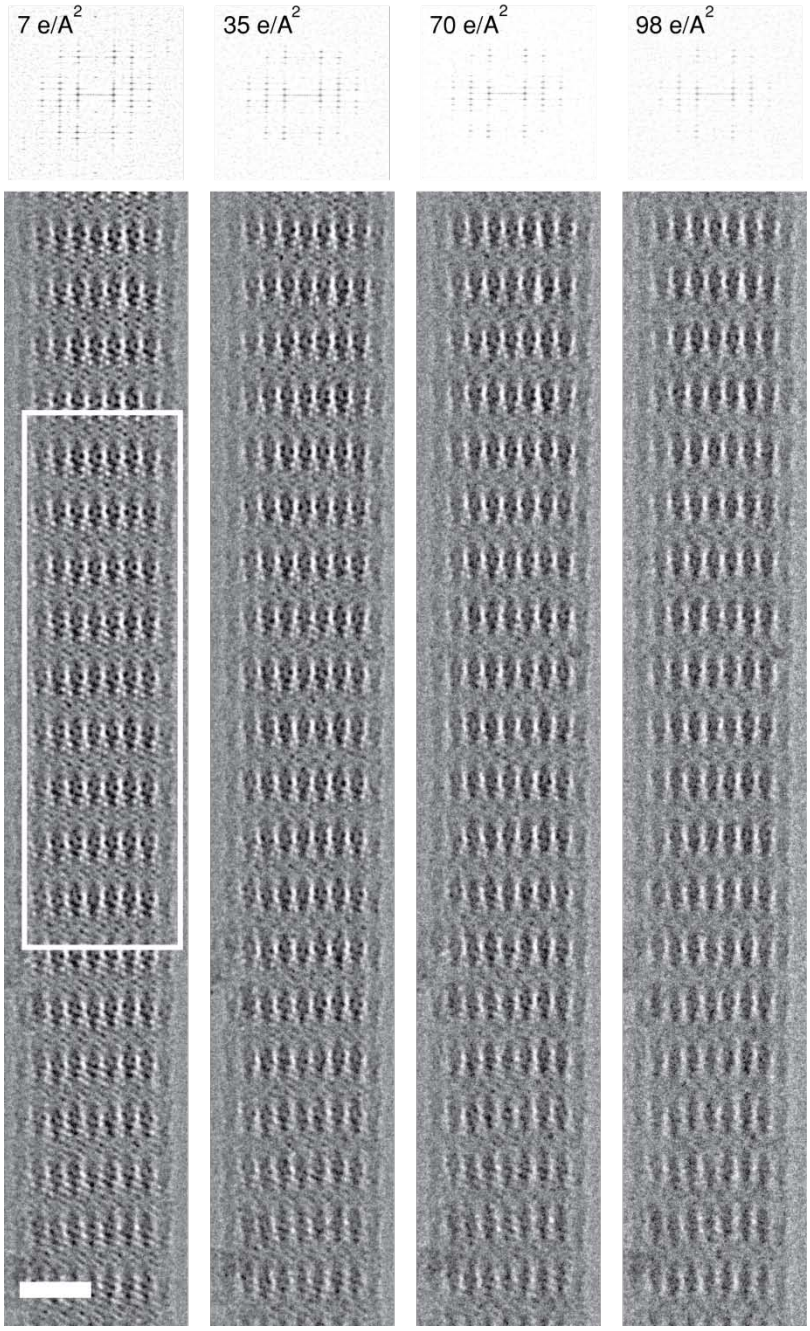

Figure S5: Corresponding images for the 120 keV cryo-data presented in Figure 2 of the main text. The square represents the area used to obtain reflections. The scale bar is 50 nm. It can be easily noted that zig-zag pattern vanishes at 98 e/A^2 .

For comparison we analyzed the damage dependent decay of two reflections at (1,13) and (2,13), with resolution values, $k = \sqrt{(k_x + k_y)}$, of 5.5 nm and 4.3 nm as shown in Figure S6.

The decay in Fourier peaks is consistent with the Figure 2 in the main text of the manuscript. Values for the decay rate at room temperature are $D^{o}_{1/e}$ (293 K)=115 ± 5 and $D^{\square}_{1/e}$ (293 K)=35 ± 3, meanwhile at 98°K the values for decay rate are $D^{o}_{1/e}$ (98 K)=62 ± 4 and $D^{\square}_{1/e}$ (98 K)=31 ± 3.

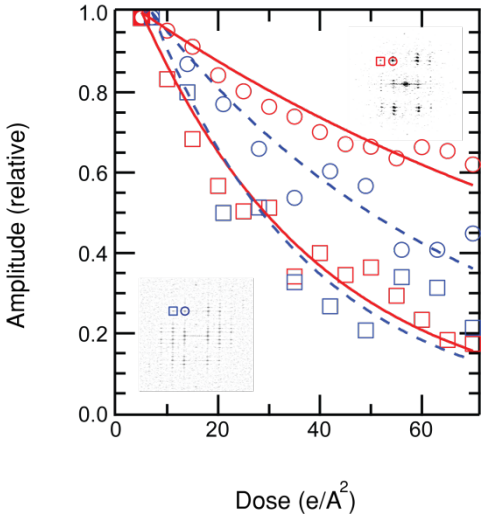

Figure S6: Radiation damage for the 4.3 nm (square) and 5.5 nm (circles) amplitudes of Fourier Amplitudes both for 98 K (blue) and room temperature (red).

Estimated comparison of free radical diffusion in the liquid and ice water: The exact nature of the temperature dependence of the secondary damage caused to biological specimens in TEM by radiation damage is poorly understood. Here, we present the possible role of free radical diffusion by estimating the flux of radical diffusing away from imaged area both in liquid (293 K) and ice (98 K) water for our experimental geometry. Typical imaging conditions used in electron microscopy when imaging protein structures are: beam diameter of $2R$~10 µm and the specimen thickness of t~100 nm Let's consider steady state diffusion in the presence of radical concentration, C(x), during the imaging. For simplicity, assume that the concentration outside the beam to be 0 and the concentration in the center of the imaging area to be C_0. Since radicals are

generated by radiolysis of water we assume that under the similar imaging conditions radical concentrations are comparable. Flux of radicals, *J*, then can be expressed as (6):

$$J = D\frac{C_0}{\delta}$$

here, δ- is roughly the length that radicals should travel to get outside the viewing area where the concentration is 0. In case of frozen specimens this distance is the specimen thickness since it is the shortest path for radicals to diffuse out into than vacuum of the microscope and therefore, δ_{ice}=t≈100 nm. However, in case of the liquid samples radicals cannot escape into the vacuum in a sealed liquid cell, hence δ should roughly be equal to a diameter of electron beam, δ_{liquid} =*R*≈5 μm. The ratio of fluxes of radicals diffusing away from the specimen in case of liquid versus ice water is:

$$\frac{J_{liquid}}{J_{ice}} = \frac{D_{liquid}t}{D_{ice}R}$$

Expressing diffusion constant as $D = D_0 \exp(^{-E_a}/_{k_B T})$, where an activation energy need for a gas molecule to hop from one lattice site to another is E_a≈1.85 kcal/mol (7), we arrive at final expression:

$$\frac{\boldsymbol{J_{liquid}}}{\boldsymbol{J_{ice}}} = \frac{\boldsymbol{t}}{\boldsymbol{\delta_{liquid}}}\mathbf{exp}\left[\frac{\boldsymbol{E_a}}{\boldsymbol{k_B}}\left(\frac{\mathbf{1}}{\boldsymbol{T_{ice}}} - \frac{\mathbf{1}}{\boldsymbol{T_{water}}}\right)\right] \approx \mathbf{1.1} \text{ (Eq. S7)}$$

As we have mentioned in the main text, the secondary damage caused by free radicals is only one of the several damage mechanisms and it will depend which damage prevails the most.

Bundle reconstruction from Fourier Transforms: The series of reconstructed acrosome images (3 unit cells) in liquid water are shown Figure S7. These images display dynamic changes to structure during of the acrosome during the drift and bending of Figure S4).

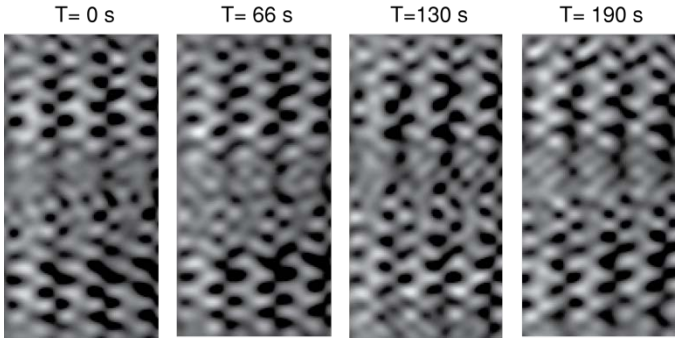

Figure S7: Two-dimensional projection maps of the acrosomal bundles in *h0l* view calculated from images in the damage series with corresponding cumulative doses of 5, 30, 60, 90 e/A^2.

Bubble Formation and Specimen Drying: When a hydrated sample at cryogenic temperatures is exposed to a high dose electron beam it is reported that ice bubbles form under cryogenic temperatures (8-10) as observed in Figure S8A. In water solution at room temperature we observe that the liquid gets pushed away at high electron beam doses and the protein gets carbonized (Figure S8B).

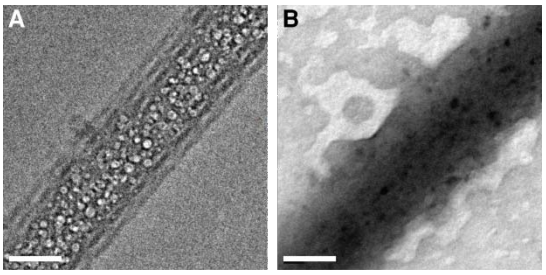

Figure S8: Radiation damage of acrosomes at high doses. (A) Formation of ice bubbles structure at 98^{o}K in vitrified sample after sample has been exposed to the electron doe 180 e/A^2. (B) Drying process of acrosomes in aqueous sample at 293 K at the electron dose of 610 e/A^2. The scale bar is 50 nm.

Supporting References:

1. Schmid, M. F., P. Matsudaira, T.-W. Jeng, J, Jakana, E. Towns-Andrews, J. Bordas, W. Chiu. 1991. *J. Mol. Biol.* 221:711-725.
2. Miller, H. P. & Wilson, L. in *Methods in Cell Biology,* L. Wilson, J. J. Correia Eds. (Elsevier Inc., New York, 2010) vol 95; pp. 3–15.
3. Henderson, R., J. M. Baldwin, …, F. Zemlin. 1986. Ultramicroscopy. 19:147-178.
4. Goldstein, J. I., J. L. Costley, G. W. Lorimer, S. J. B. Reed. 1977. *Scanning Electron Microscopy 1* (IIT Research Institute, Chicago,) pp. 315-324.
5. Williams, D. B., C. B. Carter. 2009 *Transmission Electron Microscopy: A Textbook for Material Science*. **(**Springer, New York), pp. 102-110.
6. Berg, H. C. 1993. *Random Walks in Biology.* (Princeton University Press, Princeton, NJ), pp. 15-36.
7. Teixeira, J. M.-C Bellissent-Funel, S. H. Chen, A. J. Dianoux.1984. Phys. Rev. A. 31(3):1913-1917
8. Yakovlev, S., M. Misra, S. Shi, M. Libera. 2009. *J. Microscopy*. 236:174-179.
9. Aronova, M. A., A. A. Sousa, R. D. Leapman. 2011. *Micron*. **42**:252-256.
10. Leapman, R. D., S. Sun. 1995. *Ultramicroscopy*. 59:71-79.